Full length article

Fringe slope discrimination in laser self-mixing interferometry using artificial neural network

Ke Kou*, Cuo Wang, Tianhong Lian, Jun Weng

School of Mechanical and Precision Instrument Engineering, Xi'an University of Technology, Xi'an 710048, Shaanxi, China

HIGHLIGHTS

- A method based on neural networks is proposed to identify self-mixing fringes' slope.
- Discrimination accuracy can be up to 96% in experiments without noise filtering.
- Discrimination accuracy decreases as noise increases and feedback strength reduces.
- The model trained under a certain condition is also applicable to other conditions.

ARTICLE INFO

ABSTRACT

Due to high sensitivity, self-aligned configuration and laser type independence, Laser Self-Mixing Interferometry (SMI) has always been an interesting and attractive technique in the field of laser interferometry, with displacement and vibration measurements being the most frequently encountered applications. Fringe slope is the most distinctive merit which traditional two-beam interferometry does not have, and it is always utilized to indicate the moving direction of external targets. Due to the existence of noise and even speckle effect, the slope of SMI fringes may be difficult to determine and therefore attracts much more research attention. In order to bring about a robust and easy-to-use method in fringe detection, an Artificial Neural Network (ANN) model established by a well-known Machine Learning (ML) framework named pytorch is proposed to recognize SMI fringes, and through elaborate training, it can distinguish left or right tilted unseen fringes at the accuracy of about 100% in the simulations under good Signal-to-Noise Ratio (SNR) and 96% during the experiments without any noise filtering. Relatively satisfactory results can still be obtained with the feedback strength parameter C lowed to about 0.4 and the SNR reduced to 5 dB. The manuscript explores the application of ML in the field of SMI, with a focus on the accurate and effective SMI fringe recognition, while the subsequent displacement or vibration measurement is not in our research scope.

1. Introduction

Laser Self-Mixing Interferometry (SMI) phenomenon, which was observed in the 1960s, was regarded as a detrimental factor to laser systems at the early stage and has been gradually transformed into a sensing technique since the 1980s [1–3]. Displacement or vibration measurement is the most straightforward and favorite application for SMI researchers till now, though it can also be adopted to detect distance [4], velocity [5], particle size [6] and surface profile [7]. For harmonic vibration, typical SMI signals have sinusoidal or sawtooth fringes whose slope relies on laser feedback strength and indicates vibrating direction. The slope is the inherent advantage of SMI over traditional Two Beam Interference (TBI), and both of them have the same phase sensitivity, that is, a fringe corresponding to half a wavelength displacement [8]. Therefore, the Fringe Counting Method (FCM) is the most convenient one to reconstruct external targets' movement. Of course, there is another kind of methods based on phase detection [9], which is not in the research scope of this paper.

The FCM appeared several decades ago and has been widely applied to SMI vibration measurement [10]. The general procedures always include signal differentiation and fringe judgement (transition detection) by preset threshold values. However, under noisy or speckle affected environment, these implementations are not robust enough, which often causes mis-recognition or fringe absence even with self-adaption threshold [11,12]. Norgia developed a fully analog SMI vibrometer [13], which is capable of real-time measurement but at the

expense of increasing hardware cost. Arriaga introduced a versatile and comprehensive algorithm [14] relying on basic signal processing functions such as FFT, IFFT, Hilbert transform and filtering, which results in quite complex procedures. Jiang proposed an interesting double-differential method to improve transition detection [15], whereas the influence of noise cannot be totally avoided. Bernal utilized an innovative custom-made wavelet transform for fringe detection [16], but it still cannot correctly process low-amplitude and low-feedback fringes nor run in the real-time mode. Wei employed an even-power fast algorithm to improve SMI fringe resolution [17] but he did not deal with the noise problem. Fortunately, when observing SMI signals on an oscilloscope, human eyes can easily recognize fringe slope even with severe signal noise, so a Machine Learning (ML) idea is proposed in the paper to recognize SMI fringes at high precision, which acts as an alternative yet novel and easy-to-use technique for fringe discrimination.

The manuscript merely focuses on SMI slope recognition, while the subsequent displacement reconstruction is not discussed, which can be implemented through some already published methods such as phase unwrapping. The article is organized as follows. The next section concentrates on fringe discrimination methods, covering two main procedures, namely, SMI fringe extraction and identification. The two subsequent sections are simulation and experiment to verify the distinguishing technique proposed, and two already reported methods are also included for comparison. At last, a conclusion section is drawn to tie the whole paper together and gives some potential regarding the ML in the field of SMI sensing and measurement.

2. Methods

2.1. Fringe extraction

Fringe extraction is the mandatory procedure prior to actual fringe discrimination, and the features and waveforms of typical SMI signals should be analyzed first.

Most characteristics and behaviors of SMI signals can be explained by three-mirror Fabry-Perot cavity model or time-delayed Lang-Kobayashi rate equations [18], whose power and phase variation principles are presented as Eqs. (1) and (2) [19].

$$P = P_0 [1 + m\cos(\phi_F)] \tag{1}$$

$$\phi_0 = \phi_F + C\sin(\phi_F + \arctan\alpha) \tag{2}$$

where P_0 and ϕ_0 are the optical power and the phase of the laser without laser feedback, ϕ_F is the phase under laser feedback, m is the undulation coefficient, c is the speed of light, and α is the line-width enhancement factor. C indicates the laser feedback strength parameter, as described in Eq. (3).

$$C = \frac{L}{nl} \cdot (1 - R_2) \cdot \sqrt{\frac{R_3}{R_2}} \cdot \sqrt{1 + \alpha^2} \tag{3}$$

L is the absolute distance between the laser front mirror and the reflective target, n and l are the refractive index of the gain medium and the length of the internal cavity, R_2 and R_3 are the reflectivity of the laser front mirror and the external target.

An exemplary SMI signal with a sinusoidally vibrating target is shown in the following Fig. 1, which is deduced from Eqs. (1) and (2) with C set to 0.8, the laser wavelength set to 1064 nm and the signal-to-noise ratio (SNR) set to about 25 dB. It is obviously exhibited in Fig. 1 that the SMI fringes are left or right tilted, where the right-tilted fringe (or position fringe) indicates the target is moving away from the laser, while the left-tilted one (or negative fringe) indicates that the target is approaching the laser.

The fringe extraction utilized hereafter is based on the concept that SMI fringes can be seen as local signal peaks [20]. Therefore, a peak detection approach can be used to search SMI fringes, whose flowchart is demonstrated in Fig. 2.
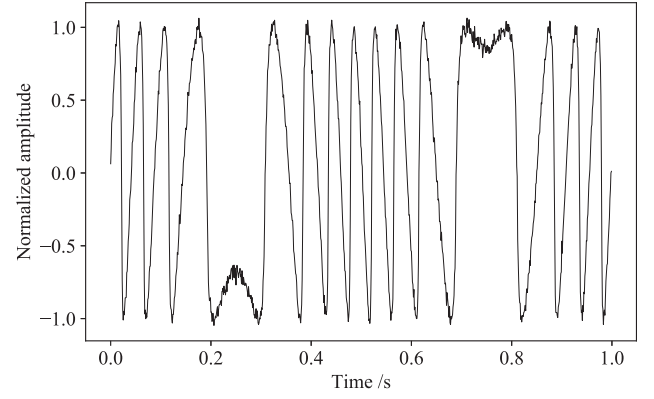

Fig. 1. Exemplary SMI signal with the external target vibrating sinusoidally.
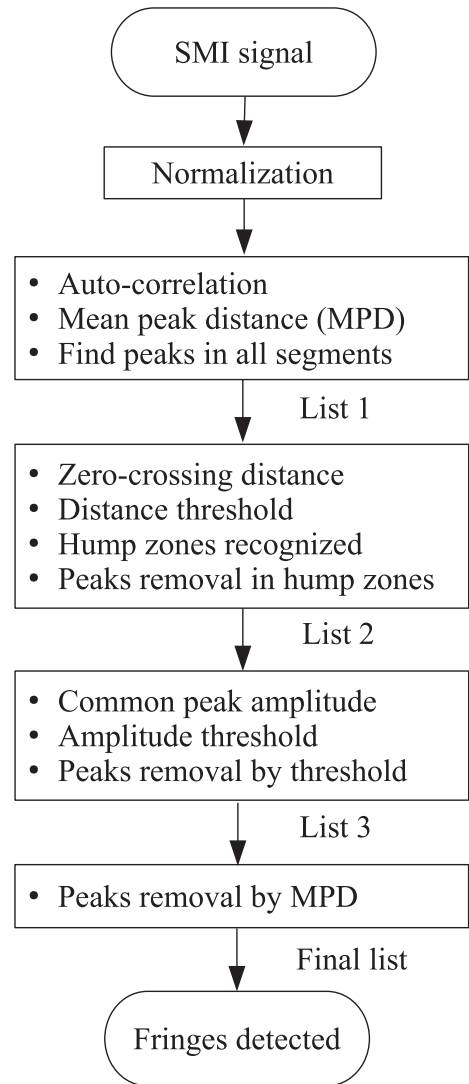
Fig. 2. Flowchart of fringe extraction.

The SMI signal should be processed in each time window one by one, which is set to one vibration period of the signal examined for convenience. Of course, in practice, the time window can be set arbitrarily as long as the number of hump zones is far smaller than that of SMI fringes, in order to minimize the influence of period variation caused by auto-correction which will be mentioned later. In each time window, the signal is firstly normalized to the range ±1 to ensure the
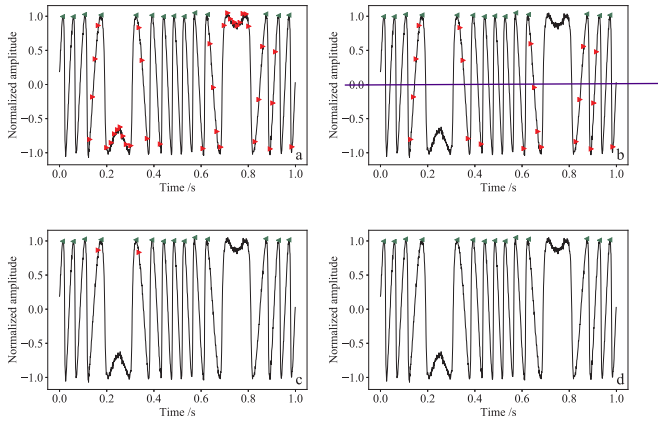
Fig. 3. Peaks indicators. [a: original peaks after find_peaks function (list 1); b: after hump zone peaks removal (list 2); c: after low-amplitude peaks removal (list3); d: true peaks after correction with MPD (final list).]

Fig. 4. Extracted fringes for example.

robustness of the fringe extraction. A parameter named mean peak distance (MPD) d is used to exclude peaks that are very close to each other. To obtain d, auto-correlation is adopted because it helps to exhibit the periodicity of the signal's fringe and partially suppress the influence of noise as the noise is always stochastic and not obviously self-correlated. After implementing auto-correction, a function from scipy library named find_peaks is utilized to search peaks of the self-correlated signal, and the MPD d is obtained from averaging all the peak distances of the self-correlated signal. Then, the normalized SMI signal in the time window is segmented into smaller parts, and adjacent parts have 25% overlap to avoid that the peak happens to appear around part borders. The find_peaks function with the distance parameter $d/4$ is applied to each part one by one, and duplicated peaks are easily recognized and discarded, which results in the first peaks location list called list 1, where a lot of false detections can also occur as the actual experimental signals contain noise and local signal variations in addition to true fringes, as shown in the following Fig. 3a. The green triangles indicate true fringes while the red triangles correspond to false ones. Here, the MPD is divided by four to serve as the distance parameter of the find_peaks function mainly due to the fact that any missed true peaks cannot be recovered from subsequent procedures.
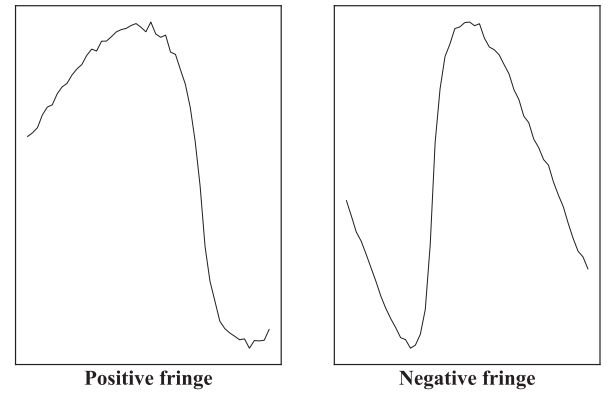
The hump zone, which indicates the directional turning point of external targets, has no true fringes and all the detections in this zone should be eliminated. Zero-crossing is a customary method to identify the hump zones of SMI signals, since the zero-crossing distance of a hump zone is generally larger than that of an ordinary fringe. All the zero-crossing points are found out when adjacent data points have opposite signs, and the largest zero-crossing distance is determined by differential, which times a factor (0.8 here) and acts as a threshold to distinguish hump zones and then remove hump zone peaks. Then, false detections in the hump zones are deleted, and the list 1 is transferred into another peak location list called list 2.

It is necessary to find out the most common peak amplitude values, multiplied with a factor (0.6 here) and used as a threshold to remove false peaks. Any peak whose amplitude is less than the threshold is considered as a false detection and then eliminated. Then, the list 2 is reduced to a new peak location list called list 3.

Finally, the correction with the MPD d is utilized to further remove false peaks, and any consecutive peaks with the distance shorter than d are compared. The peak with smaller amplitude is regarded as a false one and then removed. Then, a final peak location list with sufficiently high robustness is derived from list 3. The following fringe discrimination method totally relies on the final list here.

All the fringe extraction procedures are clearly illustrated in following Fig. 3.

Now, it is convenient to pick out fringes from normalized SMI signals, just by selecting some data whose length is shorter than general peak distance around the peak point. Two types of fringes selected are shown in Fig. 4 for instance.

2.2. Fringe identification

It is the fact that human eyes can recognize fringes' slope even with severe noise to spark the inspiration of using ML, which imitates humans' nervous system and has always been applied to classification and recognition problems in recent years. Artificial Neural Network (ANN) is the most frequently used ML model, indicating great possibility to fulfill the demand of fringe discrimination with elaborate pre-training.

The architecture of the ANN employed for the fringe classification is demonstrated in Fig. 5 below.

Here, the fringe signal itself acts as the feature vector, just because it has sufficient or even redundant information to describe the slope direction. The length of the feature vector can be preset to N ($N = 50$ in this paper without the loss of generality) and remains constant at the training and testing stages. Of course, N means the number of sampling points within a fringe. If the fringes become denser with larger vibrating amplitude or frequency, linear interpolation can be utilized to pad the fringe signal to length N. While the fringes turn sparser, data extraction is adopted instead to maintain the same signal length N.

The main function of hidden layers is feature representation, which transforms the input vector into another abstract space in order to exhibit features and achieve easy classification. The number of hidden layers and the number of neurons in each layer are merely related with the problem and cannot be obtained from definite functional relations according to the research till now. One hidden layer is selected primarily due to the fact that only one slope feature of the SMI fringe is considered, and it is generally sufficient to address this kind of
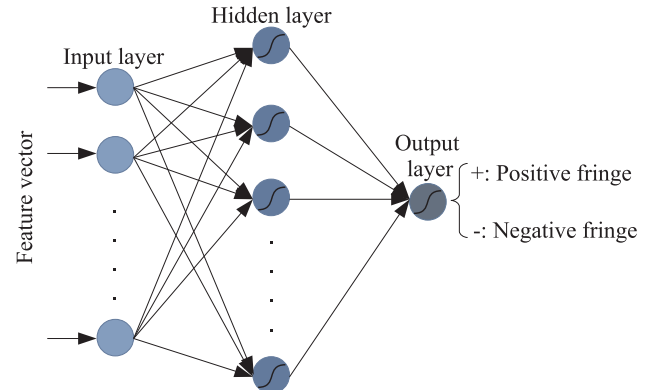
Fig. 5. The architecture of ANN employed for the classification of fringe direction in SMI signals.

classification problems. The number of neurons in the hidden layer can be preset to M (M value is determined by trials), which is a main hyper-parameter to be concerned since it definitely influences the discrimination performance and may cause critical problems such as over-fitting [21].

The activation function of the neuron is the tanh function that maps the input to the range between ±1. The output value closer to 1 indicates that the fringe tends to be a positive or right-tilted fringe, while the value closer to -1 means more possibility for the fringe to be a negative or left-tilted fringe.

The optimization method is the widely-used stochastic gradient descent technique, and the loss function is the mean squared error between the predicted outputs of the network and the labels assigned previously.

Learning rate and training times are another two hyper-parameters which primarily determine the learning speed. Both of them are preset depending on experience and will not be discussed in the following sections.

All the labels at the training stage are classified into 1 and -1 through human eye observation, which represent positive and negative fringes respectively. After the training process, the ANN can be employed to classify unseen and unlabeled SMI fringes into one of two types.

3. Simulation results

According to the methods proposed in the last section, simulation verification is implemented through the most popular ML language named python, with third party libraries numpy to complete numerical calculation as well as pytorch to establish ANNs and matplotlib to plot figures.

Given that SMI signals from moderate or strong feedback regimes always exhibit sawtooth-like fringes and have more obvious slope feature than those from the weak feedback regime, the recognition accuracy in these two regimes is always 100% and not include in the paper. so only weak feedback signals that are more difficult to recognize are considered to strictly test the performance of the proposed method.

Five segments of SMI signals with different SNRs and different C values are developed according to Eqs. (1) and (2) total of 250 fringes are extracted in each segment to perform as the data set, half of which are positive fringes and the other half are negative ones. 50 labeled fringes out of 250 SMI fringes are utilized for ANN training, while the half of the left fringes can be used for validation and the other half serves as the test set. Therefore, there are five established ANN models and their conditions are shown in Table 1.

With regard to each condition mentioned above, a ANN model is trained with the training data set and is then validated with the validation data set to find out the most suitable M value, whose results are exhibited in Table 2. A total of four M values close to the length of the feature vector are chosen for comparison, and their influence is not so obvious with better SNRs and turns to be a little bit pronounced as the SNR deteriorates and the slope reduces. M can be set to 60 to achieve the best performance based on comprehensive consideration.

After M selection, it is time to test the performance of these ANN models with the test data sets. Simultaneously, another two published methods, namely, adaptive transition detection method (ATDM) [12]

Table 1
The detailed simulation conditions.

Model	Condition details	
ANN1	SNR: 25 dB	C: 0.8.
ANN2	SNR: 10 dB	C: 0.8.
ANN3	SNR: 5 dB	C: 0.8.
ANN4	SNR: 5 dB	C: 0.6.
ANN5	SNR: 5 dB	C: 0.4.

Table 2
Validation results of five ANN models.

Model	M	Positive fringes	Negative fringes	Total fringes	Accuracy
ANN1	40	50/50	50/50	100/100	100%
	50	50/50	50/50	100/100	100%
	60	50/50	50/50	100/100	100%
	70	50/50	50/50	100/100	100%
ANN2	40	50/50	50/50	100/100	100%
	50	50/50	50/50	100/100	100%
	60	50/50	49/50	99/100	99%
	70	50/50	49/50	99/100	99%
ANN3	40	47/50	47/50	94/100	94%
	50	47/50	47/50	94/100	94%
	60	47/50	47/50	94/100	94%
	70	47/50	47/50	94/100	94%
ANN4	40	47/50	46/50	93/100	93%
	50	47/50	46/50	93/100	93%
	60	48/50	47/50	95/100	95%
	70	47/50	46/50	93/100	93%
ANN5	40	42/50	46/50	88/100	88%
	50	42/50	45/50	87/100	87%
	60	43/50	47/50	90/100	90%
	70	41/50	44/50	85/100	85%

Table 3
Detection accuracy of unseen fringes under the SNR of 25 dB and C of 0.8.

Model	M	Positive fringes	Negative fringes	Total fringes	Accuracy
ANN1	60	50/50	50/50	100/100	100%
ANN2	60	50/50	50/50	100/100	100%
ANN3	60	50/50	50/50	100/100	100%
ANN4	60	50/50	50/50	100/100	100%
ANN5	60	50/50	49/50	99/100	99%
ATDM	×	50/50	50/50	100/100	100%
DCM	×	50/50	50/50	100/100	100%

and duty-cycle method (DCM) [22], are introduced here for comparison. The performance is evaluated by accuracy, which is defined as the ratio of correctly identified fringes to the number of fringes used for testing. The results of identification are shown in Table 3. M is the number of neurons at the hidden layer as described in the last section. Where the symbol × means the method does not have this parameter. The network has high accuracy in recognizing SMI fringes and identified all the testing fringes correctly, so did the other two methods.

Other segments of SMI signals with the SNRs of 10 dB and 5 dB are utilized to further test the performance of the ANN established. The results are presented in Tables 4 and 5. Where the symbol – indicates the method failed to recognize SMI fringes. Our ANN model established under a certain condition has relatively high accuracy in recognizing SMI fringes from other conditions. An accuracy larger than 90% can be achieved even under the SNR of 5 dB, which is a terrible condition in practical measurements at labs. Of course, the accuracy is further promoted when the ANN model' training data has the same SNR as the

Table 4
Detection accuracy of unseen fringes under the SNR of 10 dB and C of 0.8.

Model	M	Positive fringes	Negative fringes	Total fringes	Accuracy
ANN1	60	48/50	47/50	95/100	95%
ANN2	60	50/50	49/50	99/100	99%
ANN3	60	48/50	48/50	96/100	96%
ANN4	60	45/50	48/50	93/100	93%
ANN5	60	47/50	46/50	93/100	93%
ATDM	×	–	–	–	–
DCM	×	47/50	45/50	92/100	92%

Table 5
Detection accuracy of unseen fringes under the SNR of 5 dB and *C* of 0.8.

Model	*M*	Positive fringes	Negative fringes	Total fringes	Accuracy
ANN1	60	43/50	47/50	90/100	90%
ANN2	60	43/50	48/50	91/100	91%
ANN3	60	46/50	47/50	93/100	93%
ANN4	60	45/50	47/50	92/100	92%
ANN5	60	45/50	43/50	88/100	88%
ATDM	×	–	–	–	–
DCM	×	42/50	43/50	85/100	85%

Table 7
Detection accuracy of unseen fringes under the SNR of 5 dB and *C* of 0.4.

Model	*M*	Positive fringes	Negative fringes	Total fringes	Accuracy
ANN1	60	43/50	42/50	85/100	85%
ANN2	60	43/50	44/50	87/100	87%
ANN3	60	47/50	40/50	87/100	87%
ANN4	60	41/50	47/50	88/100	88%
ANN5	60	46/50	44/50	90/100	90%
ATDM	×	–	–	–	–
DCM	×	40/50	40/50	80/100	80%

testing data. The well known and widely used ATDM hardly discriminates any SMI fringes, as all the transition pulses are buried in noise and cannot be found out by thresholds. The DCM worked, but its resultant accuracy is somewhat less than that of the ANN, which is attributed to the fact that the DCM depends on exact temporal positions of signal peaks and valleys while the ANN only cares about slope trends.

Subsequently, the influence of feedback strength parameter *C* is considered with the SNR held to the worst 5 dB, and *C* varies from 0.8 to 0.6 and 0.4. A reduced *C* value causes the SMI fringes to be less tilted and increases the difficulty of fringe direction discrimination. The results are demonstrated in Tables 6 and 7. Our ANN model established under a certain condition still has relatively high accuracy larger than 85% in recognizing SMI fringes with decreasing slopes. Especially when *C* reaches 0.4, the fringe signal is intrinsically not tilted and is severely polluted by noise, so its direction is hardly identified by human eyes. Of course, the accuracy is further promoted when the ANN model is trained with the data that has the same feedback strength as the testing data. The ATDM still failed due to the influence of both noise and small *C* values. The DCM worked as before, still with less accuracy than the ANN model.

After comprehensive consideration of Tables 3–7, the detection accuracy of ANN models decreases as noise increases and the feedback strength reduces. The ANN model established under a certain condition is applicable to various other working conditions with enough robustness. Best performance always occurs when the ANN model's training data has the same conditions with the testing data. Nevertheless, in actual measurement situations, SNR and C will not vary pronouncedly and frequently, so a pre-trained ANN model can be used for a relatively long period of time if the ambient environment nearly holds stationary. The ANN model shows better accuracy when compared with these two reported methods, and all the results exhibited above are beneficial to designing the experimental ANN and will provide guidance for the experiment validation below.

Considering the completeness of the method proposed, the signals with *C* smaller than 0.4 are also tested, and the results are shown in Table 8 below. when *C* is lowed beyond 0.4, fringes' slope is not sufficient to retain high recognition accuracy no matter what's the SNR level, and the accuracy values falls sharply below 80%. Thus, the lower *C* limit of the technique proposed is approximately 0.4 here. Additionally, the time performance of the ANN model has also been tested. After pre-training and with *M* set to 60, the model can obtain the

Table 8
Detection accuracy of unseen fringes with *C* smaller than 0.4.

SNR	*C*	*M*	Positive fringes	Negative fringes	Total fringes	Accuracy
25 dB	0.3	60	40/50	40/50	80/100	80%
	0.2	60	34/50	36/50	70/100	70%
	0.1	60	22/50	30/50	52/100	52%
10 dB	0.3	60	35/50	38/50	73/100	73%
	0.2	60	34/50	34/50	68/100	68%
	0.1	60	25/50	30/50	55/100	55%
5 dB	0.3	60	40/50	35/50	75/100	75%
	0.2	60	35/50	29/50	64/100	64%
	0.1	60	30/50	26/50	56/100	56%

discrimination results of 100 SMI fringes within about 2 ms (Intel Core i7-6700HQ CPU @2.60 GHz 2.60 GHz and 8 GB RAM), which satisfies the requirement of some general applications but still needs improvements for most real-time measurements.

4. Experimental results

Experimental configuration employed for SMI slope recognition is depicted in the following Fig. 6 [23]. The SMI configuration utilized here is not the most typical one, which often merely includes a laser diode (LD) packaged with a built-in photodiode (PD) and an external target. The typical structure has the merits of compactness, low-cost and easy operation. Nevertheless, a more complex and higher cost setup based on Solid-State Laser (SSL) is still utilized here primarily due to that we mainly concern about detection sensitivity other than miniaturization and cost. As reported in [24], SSLs always have higher detection sensitivity to feedback light than LDs, as a SSL's fluorescence to photon lifetime ratio is generally two or three orders of magnitude higher than that of a LD.

In our experimental configuration, a microchip SSL is adopted with the laser crystal of Nd:YAG, which has round shape with the diameter of 10 mm, the thickness of 0.75 mm and the doping concentration of 1.2%. The pumping facet of the Nd:YAG is coated by a high transmittance film at 808 nm and a high reflectance film at 1064 nm, and the

Table 6
Detection accuracy of unseen fringes under the SNR of 5 dB and *C* of 0.6.

| Model	*M*	Positive fringes	Negative fringes	Total fringes	Accuracy
ANN1	60	45/50	45/50	90/100	90%
ANN2	60	46/50	44/50	90/100	90%
ANN3	60	46/50	46/50	92/100	92%
ANN4	60	47/50	46/50	93/100	93%
ANN5	60	43/50	47/50	90/100	90%
ATDM	×	–	–	–	–
DCM	×	45/50	40/50	85/100	85%
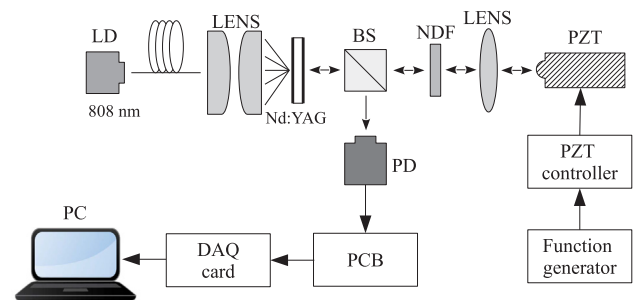
Fig. 6. Experimental setup for SMI fringe discrimination. (LD: Laser diode; BS: Beam splitter; NDF: Neutral Density Filter; PZT: Piezoelectric transducer; PD: Photodiode; DAQ: Data acquisition).
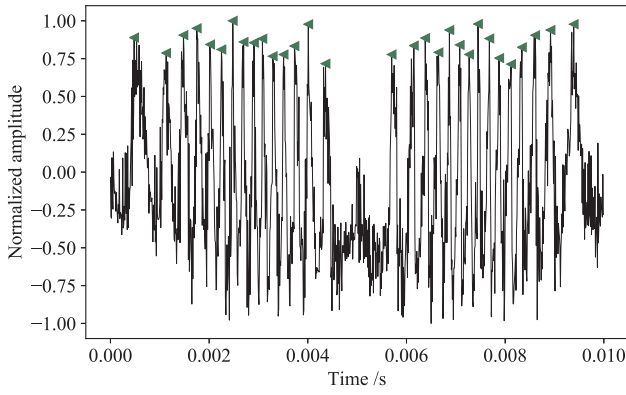
Fig. 7. Experimental SMI signal with the external PZT vibrating sinusoidally at the amplitude of 4.5 μm and the frequency of 100 Hz.
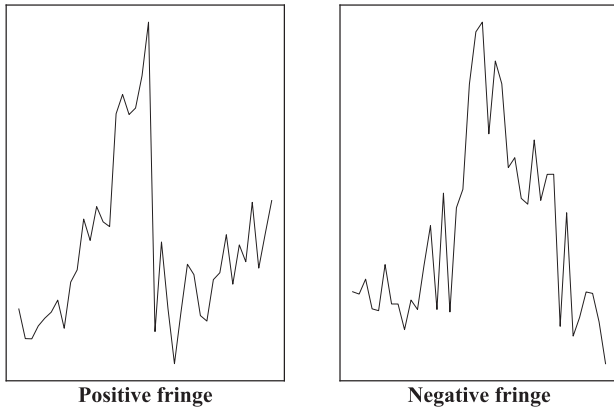
Fig. 8. Extracted fringes in the experiment for example.

Table 9
Training data conditions for each ANN model.

Model	Condition details
ANN6	Signals after digital filtering Low-pass, cut-off frequency: 20 kHz SNR: 16 dB, *C*: close to 1
ANN7	Raw signals without the NDF. SNR: 10 dB, *C*: close to 1
ANN8	Raw signals after the NDF inserted SNR: 10 dB, *C*: reduced to about 0.5

emitting facet is coated by a high reflectance film at 808 nm and a 5% transmittance film at 1064 nm. A LD with the wavelength of 808 nm acts as the pumping source. A BS is utilized to split the laser beam for optical power detection. A NDF, with a rectangular shape and a gradually decreasing transmittance along one side, is inserted in the configuration to adjust the feedback strength. The external target is a PZT stage (Thorlabs, PE4) driven by a high voltage piezoelectric controller (Thorlabs, MDT694B), whose controlling signal comes from a function generator, thus the PZT vibrates in sinusoidal waveforms with the frequency less than 200 Hz (upper bound of the bandwidth of the PZT) and the peak-peak amplitude less than 15 μm (moving range of the PZT) during the whole experiment. The signal conditioning circuit only has a current-to-voltage converter, without any hardware signal-conditioning including amplifying and filtering, to maintain the signals' original waveforms, which is advantageous to testing the model's performance without any noise removal. All the SMI signals are sampled through a 16-bit data acquisition card (USB-61902, JYTEK, China) to a PC at the sampling rate of 100 kHz.

An exemplary SMI signal in the experiment after normalization is

Table 10
Validation results of three ANN models in the experiment.

Model	*M*	Positive fringes	Negative fringes	Total fringes	Accuracy
ANN6	40	49/50	50/50	99/100	99%
	50	49/50	50/50	99/100	99%
	60	49/50	50/50	99/100	99%
	70	49/50	50/50	99/100	99%
ANN7	40	47/50	48/50	95/100	95%
	50	47/50	49/50	96/100	96%
	60	47/50	49/50	96/100	96%
	70	47/50	49/50	96/100	96%
ANN8	40	47/50	46/50	93/100	93%
	50	48/50	45/50	93/100	93%
	60	47/50	48/50	95/100	95%
	70	47/50	45/50	92/100	92%

Table 11
Detection accuracy of unseen fringes after digital filtering.

Model	*M*	Positive fringes	Negative fringes	Total fringes	Accuracy
ANN6	60	49/50	50/50	99/100	99%
ANN7	60	50/50	49/50	99/100	99%
ANN8	60	49/50	47/50	96/100	96%
ATDM	×	49/50	49/50	98/100	98%
DCM	×	49/50	48/50	97/100	97%

Table 12
Detection accuracy of unseen fringes of raw SMI signals.

Model	*M*	Positive fringes	Negative fringes	Total fringes	Accuracy
ANN6	60	45/50	49/50	94/100	94%
ANN7	60	49/50	47/50	96/100	96%
ANN8	60	46/50	47/50	93/100	93%
ATDM	×	–	–	–	–
DCM	×	44/50	46/50	90/100	90%

Table 13
Detection accuracy of unseen fringes of raw SMI signals with the feedback strength reduced by the NDF.

Model	*M*	Positive fringes	Negative fringes	Total fringes	Accuracy
ANN6	60	46/50	46/50	92/100	92%
ANN7	60	48/40	43/50	91/100	91%
ANN8	60	46/50	47/50	93/100	93%
ATDM	×	–	–	–	–
DCM	×	42/50	41/50	83/100	83%

shown in Fig. 7, and all the peaks are labeled by green triangles with the fringe extraction method mentioned above. Firstly, some dominant spike noise has been easily removed from raw SMI signals by threshold, in order to make the normalization more reasonable and the subsequent zero-crossing and hump zone detection more effective. Then, the SMI signal has been normalized through subtracting its average value and then mapping it into the range of ±1, just like those shown in Figs. 1 and 3. The fringes are distinctly tilted and there's no hysteresis phenomenon in the signal. Thus, the feedback strength parameter *C* in the experiment is evaluated to be close to 1. The SNR of this signal can be evaluated to be about 10 dB with two individual assessments when the PZT is firstly fixed and then vibrating. Following Fig. 8 exhibits two typical experimental fringes extracted using the method mentioned in Section 2.1.

Three data sets with different SNRs and different feedback strengths are obtained for experimental validation. Similar to the simulation,

each data set has 250 fringes, half of which are positive fringes and the other half are negative ones. 50 labeled fringes out of 250 SMI fringes are utilized for ANN training, while the half of the left fringes is used for validation and the other half serves as the test set. Three ANN models are established according to these data sets and their conditions are shown in Table 9. Simultaneously, the ATDM and the DCM are still utilized in the experiment for comparison.

Validation data sets, similar to those in the simulation section, are also employed for M selection, and the results are presented in Table 10. A total of four M values close to the length of the feature vector are still chosen for comparison, and their influence resembles what happens in the simulation, that is, exhibiting little effect under good SNR and becoming slightly more significant when the noise increases and the slope decreases. The best overall performance is obtained when M reaches 60.

Then, the testing procedure is implemented relying on the test sets and the corresponding results of identification are shown in Tables 11–13. The model established under a certain condition can still be applicable to other situations when the noise and the feedback strength varies. Of course, higher accuracy can be achieved if the ANN model is trained with the data that has the same conditions as the testing data. The ATDM cannot recognize SMI fringes from the raw sampled signals which are severely polluted by noise. The DCM, however, can find out most fringes correctly, but its accuracy is still worse than that of the ANN model proposed.

All the experimental results presented above follow the similar disciplines with those shown in Section 3, which validates the effectiveness and robustness of the ANN in discriminating SMI fringes, even under noisy conditions. Through elaborate data training, the method proposed has great potential to be applied in the field of SMI displacement and vibration measurements.

5. Conclusion

The paper primarily focuses on the discrimination of SMI fringes by the ANN model, which is the most commonly used model in the domain of ML. Fringe signals are firstly extracted by local peak finding, and then they are labeled by human eyes and sent to train the ANN. Identification results demonstrate that left or right tilted unseen fringes can be distinguished at the accuracy of about 100% in the simulations under good SNR and at the accuracy of 96% in the experiments without any noise filtering. The accuracy decreases as the noise increases and the feedback strength reduces. The technique mentioned is easily applicable to moderate and strong feedback regimes, and in weak feedback regime, it exhibits good performance when C is greater than 0.4. On the whole, it shows great potential to be utilized in SMI vibration measurement due to high anti-noise ability, and the application of ML or even Deep Learning (DL) to precision measurement may provide some new ideas and some benefits for sensors or instruments community, which deserves much more attention and elaborate exploration. Considering measurement is intrinsically a mapping between a sampled signal and an estimated value, future works may concentrate on directly evaluating vibration or absolute distance from SMI signals depending on the concept of ML.

CRediT authorship contribution statement

Ke Kou: Writing - original draft, Writing - review & editing, Methodology. **Cuo Wang:** Software, Visualization, Methodology. **Tianhong Lian:** Conceptualization, Data curation, Formal analysis. **Jun Weng:** Writing - review & editing.

Declaration of Competing Interest

The authors declare that they have no known competing financial interests or personal relationships that could have appeared to influence the work reported in this paper.

References

[1] S. Donati, M. Norgia, Overview of self-mixing interferometer applications to mechanical engineering, Opt. Eng. 57 (5) (2018) 051506, https://doi.org/10.1117/1.OE.57.5.051506.

[2] J. Li, H. Niu, Y. Niu, Laser feedback interferometry and applications: a review, Opt. Eng. 56 (5) (2017) 050901.

[3] T. Taimre, M. Nikolic, K. Bertling, Y.L. Lim, T. Bosch, A.D. Rakic, Laser feedback interferometry: a tutorial on the self-mixing effect for coherent sensing, Adv. Opt. Photonics 7 (3) (2015) 570, https://doi.org/10.1364/AOP.7.000570.

[4] W. Sun, H. Gui, P. Zhang, S. Wu, Z. Li, K. Zhang, Measuring millimeter-scale distances in a laser self-mixing velocimeter with low-speed wavelength modulation, Opt. Commun. 427 (2018) 107–111, https://doi.org/10.1016/j.optcom.2018.06.034.

[5] B. Gao, C. Qing, H. Li, C. Jiang, P. Chen, Rotation speed measurement based on self-mixing speckle interference, Opt. Commun. 428 (2018) 110–112, https://doi.org/10.1016/j.optcom.2018.07.056.

[6] V. Contreras, J. Lönnqvist, J. Toivonen, Detection of single microparticles in airflows by edge-filter enhanced self-mixing interferometry, Opt. Express 24 (8) (2016) 260908.

[7] K. Zhu, Y. Lu, S. Zhang, H. Ruan, S. Usuki, Y. Tan, Ultrasound modulated laser confocal feedback imaging inside turbid media, Opt. Lett. 43 (6) (2018) 1207–1210, https://doi.org/10.1364/OL.43.001207.

[8] C. Kim, C. Lee, K. O, Effect of linewidth enhancement factor on fringe in a self-mixing signal and improved estimation of feedback factor in laser diode, IEEE Access 7 (2019) 28886–28893, https://doi.org/10.1109/ACCESS.2018.2883475.

[9] C. Jiang, X. Wen, S. Yin, Y. Liu, Multiple self-mixing interference based on phase modulation and demodulation for vibration measurement, Appl. Opt. 56 (4) (2017) 1006–1011, https://doi.org/10.1364/AO.56.001006.

[10] M. Norgia, S. Donati, A displacement-measuring instrument utilizing self-mixing interferometry, IEEE Trans. Instrum. Meas. 52 (6) (2003) 1765–1770, https://doi.org/10.1109/TIM.2003.820451.

[11] H. Zhen, L. Chengwei, L. Songquan, Z. Zhenghe, L. Dongyu, Speckle affected fringe detection based on three envelope extraction for self-mixing displacement measurement, Opt. Commun. 392 (2017) 100–108, https://doi.org/10.1016/j.optcom.2017.01.037.

[12] U. Zabit, T. Bosch, F. Bony, Adaptive transition detection algorithm for a self-mixing displacement sensor, IEEE Sens. J. 9 (12) (2009) 1879–1886, https://doi.org/10.1109/JSEN.2009.2031496.

[13] M. Norgia, A. Pesatori, Fully analog self-mixing laser vibrometer, in: 2011 IEEE International Instrumentation and Measurement Technology Conference, IEEE, Hangzhou, China, 2011, pp. 1–4. doi:10.1109/IMTC.2011.5944179.

[14] A.L. Arriaga, F. Bony, T. Bosch, Real-time algorithm for versatile displacement sensors based on self-mixing interferometry, IEEE Sens. J. 16 (1) (2016) 195–202, https://doi.org/10.1109/JSEN.2015.2478755.

[15] C. Jiang, C. Li, Y. Wang, Improved transition detection algorithm for a self-mixing displacement sensor, Optik Int. J. Light Electr. Opt. 127 (14) (2016) 5603–5612, https://doi.org/10.1016/j.ijleo.2016.03.066.

[16] O.D. Bernal, H.C. Seat, U. Zabit, F. Surre, T. Bosch, Robust detection of non-regular interferometric fringes from a self-mixing displacement sensor using Bi-wavelet transform, IEEE Sens. J. 16 (22) (2016) 7903–7910, https://doi.org/10.1109/JSEN.2016.2599702.

[17] Z. Wei, W. Huang, J. Zhang, X. Wang, H. Zhu, T. An, X. Yu, Obtaining scalable fringe precision in self-mixing interference using an even-power fast algorithm, IEEE Photonics J. 9 (4) (2017) 1–11, https://doi.org/10.1109/JPHOT.2017.2717947.

[18] R. Lang, K. Kobayashi, External optical feedback effects on semiconductor injection laser properties, IEEE J. Quantum Electron. 16 (3) (1980) 347–355, https://doi.org/10.1109/JQE.1980.1070479.

[19] M. Veng, J. Perchoux, F. Bony, Fringe disappearance in self-mixing interferometry laser sensors: model and application to the absolute distance measurement scheme, IEEE Sens. J. 19 (14) (2019) 5521–5528, https://doi.org/10.1109/JSEN.2019.2901125.

[20] M. Usman, U. Zabit, O.D. Bernal, G. Raja, T. Bosch, Detection of multimodal fringes for self-mixing-based vibration measurement, IEEE Trans. Instrum. Meas. (2019) 1–10, https://doi.org/10.1109/TIM.2019.2895928.

[21] U. Zabit, K. Shaheen, M. Naveed, O.D. Bernal, T. Bosch, Automatic detection of multimodality in self-mixing interferometer, IEEE Sens. J. 18 (22) (2018) 9195–9202, https://doi.org/10.1109/JSEN.2018.2869771.

[22] A. Magnani, A. Pesatori, M. Norgia, Novel displacement reconstruction method for vibration measurements, in: 2011 IEEE International Instrumentation and Measurement Technology Conference, IEEE, Hangzhou, China, 2011, pp. 1–4. doi:10.1109/IMTC.2011.5944148.

[23] K. Otsuka, Self-mixing thin-slice solid-state laser metrology, Sensors 11 (2) (2011) 2195–2245, https://doi.org/10.3390/s110202195.

[24] K. Kou, C. Wang, J. Weng, Influence of fluorescence to photon lifetime ratio on detection sensitivity in laser self-mixing interferometry, IEEE Access 8 (2020) 10426–10432, https://doi.org/10.1109/ACCESS.2020.2963988.